Modeling Doxorubicin Pharmacokinetics in Multiple Myeloma Suggests Mechanism of Drug Resistance

Modeling Doxorubicin Pharmacokinetics in Multiple Myeloma Suggests Mechanism of Drug Resistance

Roya Doshmanziari, Francesco Da Ros, Mario Mazzucato, Morten Gram Pedersen, Roberto Visentin

Abstract*—*Objective: **Multiple myeloma (MM) is a plasma cell malignancy often treated with chemotherapy drugs. Among these, doxorubicin (DOXO) is commonly employed, sometimes in combined-drug therapies, but it has to be optimally administered in order to maximize its efficacy and reduce possible side effects. To support DOXO studies and treatment optimization, here we propose an experimental/modeling approach to establish a model describing DOXO pharmacokinetics (PK) in MM cells.** ***Methods:*** **A series of *in vitro* experiments were performed in MM1R and MOLP-2 cells. DOXO was administered at two dosages (200 nM, 450 nM) at t=0 and removed at t=3 hrs. Intracellular DOXO concentration was measured via fluorescence microscopy during both drug uptake (t=0–3 hrs) and release phases (t=3–8 hrs). Four PK candidate models were identified, and were compared and selected based on their ability to describe DOXO data and numerical parameter identification.** ***Results:*** **The most parsimonious model consists of three compartments describing DOXO distribution between the extracellular space, the cell cytoplasm and the nucleus, and defines the intracellular DOXO efflux rate through a Hill function, simulating a threshold/saturation drug resistance mechanism. This model predicted DOXO data well in all the experiments and provided precise parameter estimates (mean $\pm$ standard deviation coefficient of variation: $15.8 \pm 12.2\%$).** ***Conclusions:*** **A reliable PK model describing DOXO uptake and release in MM cells has been successfully developed.** ***Significance:*** **The proposed PK model, once integrated with DOXO pharmacodynamics, has the potential of allowing the study and the optimization of DOXO treatment strategies in MM.**

***Index Terms*—Cancer therapy, chemotherapy drug, compartmental modeling, drug resistance, feedback, system identification.**

I. Introduction

Multiple myeloma (MM) is a blood cancer of monoclonal plasma cells in the bone marrow. It represents the second most common haematological malignancy in high-income countries, with a median age of about 70 years and a 126% global incidence increase from 1990 to 2016 as a consequence of population aging [1], [2]. MM can target several areas of the body, such as pelvis, ribs, skull and spine, and its risk factors include chronic inflammation, inherited genetic variants, exposure to radiation or chemicals, and history of monoclonal gammopathy of undetermined significance [3], [4].

The process of MM diagnosis is long, complicated and discouraging for the patients, since it shows no early-stage symptoms [5]. Treatment with drugs, in addition to possible early-stage MM detection, can help to improve survival rates.

Among the available anticancer drugs, doxorubicin (DOXO) is a well established treatment in MM, as well as in breast cancer and ovarian cancer [6]–[8], though it can come with side effects such as heart failure, myelosuppression, infections and risk of relapse [1], [9], [10]. Therefore, it is evident that treatment with DOXO has to be optimized in terms of dose regimen (i.e., amount and time of administration), in order to maximize drug efficacy and mitigate its side effects, e.g. [11].

In this regard, mathematical modeling of pharmacokinetic (PK) and pharmacodynamic (PD) represents a valid approach to understand cell response to the drug. In fact, studying and integrating PK/PD models are important steps for understanding drug exposure/response, thus allowing dosing regimen optimization and providing guidance for clinical studies (e.g., suggesting an optimal dose range for treatment efficacy, or discarding in advance ineffective or potentially dangerous drug amounts). This idea has recently been proved to be successful in the study and treatment of solid tumors, e.g., [12]–[17]. For example, in the context of breast cancer a coupled experimental/modeling approach was used to develop an *in silico* PK/PD model to describe how a certain DOXO regimen impacts on cell population dynamics [12]. Furthermore, a multiscale mathematical modeling approach integrating various types of patient-specific data was proposed in [14] as a new step towards individualized tumor therapies. Similar studies were done focusing on PK/PD dose-effect synergy modeling for non small cell lung cancer and predict the lung tumor growth curves [16], [17].

Given the significant research efforts in the development of DOXO PK, it is crucial to acknowledge the heterogeneity observed among different tumors, so that it is very likely that although a PK model can accurately describe DOXO distribution in a specific cancer, it might be unsuitable for other tumors. For instance, the models developed in [12] and [16] relate to breast and lung cancers, respectively, and their structure is different. Currently, there is a lack of a comparable approach in the field of MM research, which

Manuscript received on January 24th, 2023. This work was supported by Department of Information Engineering, University of Padova, under the project SID 2020. No other potential conflict relevant to this article was reported. A preliminary version of the work was presented at the 43rd Annual International Conference of the IEEE Engineering in Medicine & Biology Society (EMBC) Oct 31 - Nov 4, 2021. Virtual Conference. R. Doshmanziari and F. Da Ros contributed equally to this work.

R. Doshmanziari is with the Norwegian University of Science and Technology, Trondheim, Norway. F. Da Ros and M. Mazzucato are with Aviano National Cancer Institute, Aviano, Italy. M.G. Pedersen and R. Visentin (corresponding author: visentin@dei.unipd.it) are with the Department of Information Engineering, University of Padova, Padova, Italy.

serves as inspiration for our long-term mission, which is to create a simulation model to support DOXO treatment optimization in MM patients.

Here we aim at developing a mathematical model able to describe DOXO PK in MM cells, investigating the generalizability and interpretability of the model candidates. This will be done by adopting a coupled experimental/model identification approach to find, among possible candidates, the model that best describes DOXO concentration data measured in two different MM cell lines. In particular, taking advantage of the fluorescence property of DOXO [18], we will analyze cell images acquired with fluorescence microscopy in order to obtain the intracellular drug concentration. Then, we will start from the available PK model [12], and we will then modify it to take possible drug resistance effects inherent to MM cells into account.

The paper is structured as follows: Section II describes the experiment setup and data collection, Section III presents the compartmental model candidates, Section IV outlines the corresponding model identification and validation, Section V shows the results and Sections VI and VII provides discussions with closing remarks and future research directions.

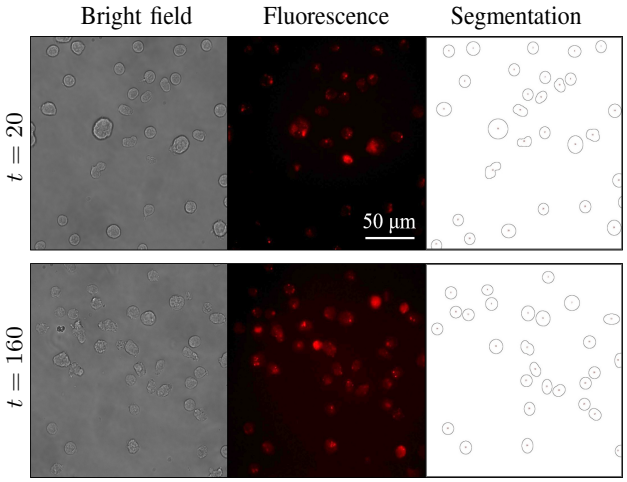

Figure 1: Illustrative cell image processing, i.e., acquired bright-field (*left*), fluorescence (*middle*) and segmented cell boundaries (*right*), performed at $t = 20$ min (*upper*) and $t = 160$ min (*lower panels*) after administration of DOXO 450 nM in MM1R cells.

II. Experiments and data collection

A. Cell culture

DOXO PK was studied in the two human cell lines MM1R and MOLP-2 [19], [20]. The MM1R cell line was established from peripheral blood of a 42-year-old MM patient who had become resistant to steroid-based therapy, and was obtained from American Type Culture Collection (ATCC, http://www.atcc.org). The MOLP-2 cell line was established from the peripheral blood of a 55-year-old man with IgD lambda type MM, and was obtained from Leibniz Institute DSMZ-German Collection of Microorganisms and Cell Cultures (DSMZ, https://www.dsmz.de/). MM1R and MOLP-2 cell lines were chosen based on their extensively researched and widely acknowledged correlation with tumors found in patients diagnosed with MM in terms of their transcriptional profiles [21]. Cells were cultured with a density of 5×10^5 cells/mL, as per MM cell culturing standards [19], [20], in Roswell Park Memorial Institute (RPMI) 1641 medium supplemented with 1% penicillin/streptomycin and 10% or 20% fetal bovine serum (FBS), for MM1R and MOLP-2 , respectively.

B. Doxorubicin treatment and image acquisition

In order to monitor DOXO uptake, we exploited its autofluorescence property (i.e., excitation of 470 nm, emission of 570 nm [18]), and measured it using a fluorescence microscope (Nikon® Eclipse T1-U).

Specifically, for both MM1R and MOLP-2, 2.5×10^5 cells were suspended in 500 µL of phosphate buffered saline (PBS), FBS 20%, at $37°$C and were treated with DOXO for 3 hrs at two concentrations, i.e., 200 nM or 450 nM, respectively. These amounts were chose to allow an easy detection with fluorescence microscopy and, at the same time, to avoid any early drug-induced cell death. For each experiment, DOXO was administered at time $t = 0$ hr. Immediately after DOXO administration, 200 µL containing 10^5 cells were drawn and seeded in double (i.e., 100 µL with 5×10^4 cells each) into two µ-Slide VI $^{0.4}$ wells (ibidi GmbH, Gräfelfing, DE).

Four-to-five images/well were acquired at 40x for both bright-field and fluorescence (Fig. 1). Image acquisition was repeated every 20 minutes for 3 hrs. At $t = 3$ hrs, the remaining cells were centrifuged for DOXO removal. After an additional washing, cell pellet was re-suspended in 300 µL of PBS, 20% FBS, to obtain a density of 5×10^4 cell/100 µL. Then, 300 µL containing 1.5×10^5 cells were drawn and seeded in triplicate (i.e., 100 µL with 5×10^4 cells each) into three µ-Slide VI $^{0.4}$ wells. Four-to-five images/well were acquired at 40x for both bright-field and fluorescence at $t = [3.5, 4, 4.5, 5, 5.5, 6, 7, 8]$ hrs. It is worth mentioning that the total number of cells as well as the total amount of medium were used to allow duplicate or triplicate measurement of DOXO concentration. Moreover, the 20 min sampling during the uptake phase allowed no more than two DOXO acquisitions at each time point due to the experimental procedure, while a triplicate collection was possible during the release phase, for which at least 30 min elapsed between two consecutive time samples.

C. Doxorubicin image processing

Prior to cell image processing, a standard curve was generated to convert DOXO fluorescence intensity into concentration values. Specifically, µ-Slide VI$^{0.4}$ wells were loaded with serial DOXO known concentrations (*C*), from 100 nM to 1600 nM, and the respective fluorescence intensity was acquired using the same microscope settings described above. Each acquired image was processed by ImageJ software [22] to obtain a measure of fluorescence intensity (*Int*), from which the background signal (corresponding to a null DOXO concentration) was removed. Finally, a linear regression model was fit

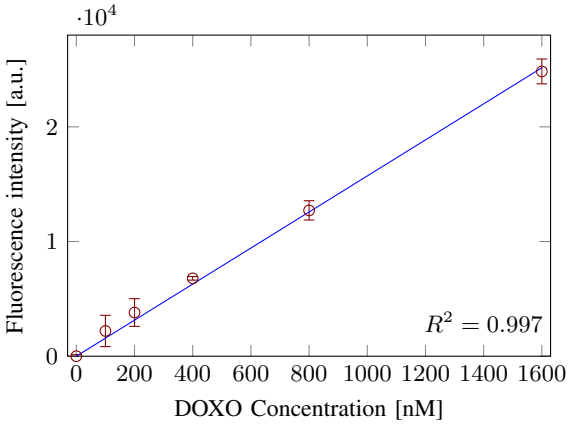

Figure 2: Linear regression model to estimate DOXO concentration from Fluorescence intensity. The goodness of model fit is provided by the coefficient of determination $R^2 = 0.997$. $n = 3$ readings for each concentration.

on *C-Int* data (Fig. 2), thus obtaining the equation describing the relationship between DOXO fluorescence intensity [a.u.] (arbitrary unit) and its concentration [nM]:

$$Int = 15.26 \cdot C \tag{1}$$

In order to obtain intracellular DOXO concentration from treatment experiments, each acquired cell image was processed by ImageJ. In particular, for each image, cell boundaries were identified via segmentation, realized through a threshold-based approach on the bright-field image (Fig. 1). The resulting mask was used with *Analyze Particles* command for measuring cell fluorescence intensity in the corresponding florescence image. A background correction was applied to cell fluorescence intensity to exclude free DOXO contribution. Finally, cell fluorescence intensity was converted to concentration value by reversing the equation (1).

III. Modeling Doxorubicin PK

Following DOXO administration to a cell culture, intracellular concentration is supposed to rise with a certain kinetics. On the other hand, after its removal, DOXO is likely to exit from the intracellular back to the extracellular space, if not bound to the DNA. Such a description has been proposed to model DOXO PK in breast cancer [12]. However, the heterogeneity among cancer types does not guarantee that the same model is suitable for describing DOXO PK in MM, as demonstrated in a preliminary study [23]. Thus, we propose several model candidates for describing DOXO PK in MM cells, with different functional relationships. The basic assumption, common for all the model structures, is that drug PK involves both extracellular and intracellular spaces.

Model I: The first model, introduced in [12] and schematized in Fig. 3a, describes DOXO PK with a three-comparmental structure of equations (2) and (3):

$$\begin{cases} \dot{X}_E(t) = k_{EF}\frac{V_I}{V_E}X_F(t) - k_{FE}X_E(t) + u(t) \\ \dot{X}_F(t) = k_{FE}\frac{V_E}{V_I}X_E(t) - k_{EF}X_F(t) - k_{BF}X_F(t) \\ \dot{X}_B(t) = k_{BF}X_F(t) \end{cases} \tag{2}$$

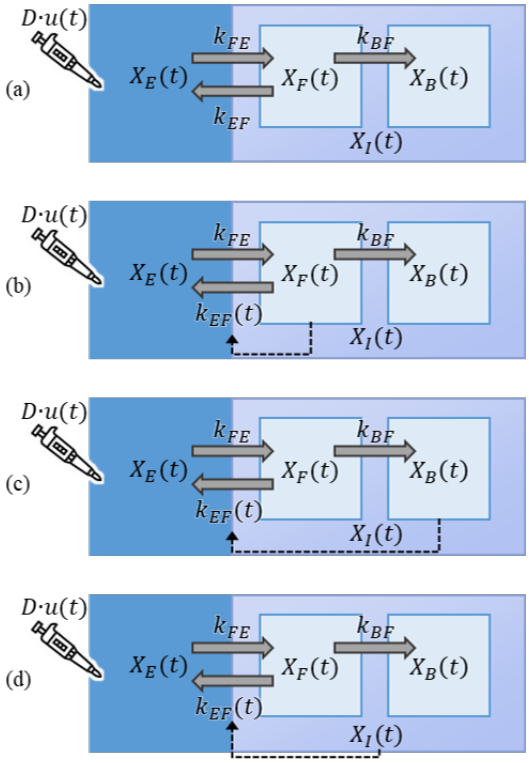

Figure 3: Schematic diagrams of *Models I* (a), *II-IV* (b, c and d). D (nM), dose amount of DOXO administered at $t = 0$; X_E, X_I, X_F, X_B, (nM), DOXO concentration in the extracellular and intracellular (divided into free and bound) space, respectively; k_{FE}, k_{EF}, k_{BF} (hr^{-1}), rate constant parameters; $k_{EF}(t)$ (hr^{-1}), defined as a time-varying parameter depending on $X_i : \{X_F, X_B, X_I\}$ in models II-IV (b, c and d).

$$X_I(t) = X_F(t) + X_B(t) \tag{3}$$

where $X_E(t)$ and $X_I(t)$ are the extracellular and intracellular DOXO concentration (nM), respectively; $X_F(t)$ is the concentration of free intracellular DOXO diffused into the cell; $X_B(t)$ is the concentration of DOXO bound to the DNA inside the cell nucleus; k_{FE}, k_{EF}, k_{BF} (hr^{-1}) are constant rate parameters, assumed to be independent from drug dosage and exposure time, describing DOXO transit from extracellular to free intracellular, from free intracellular to extracellular, and from free intracellular to bounded compartment, respectively; V_E and V_I are the volumes of the extracellular and intracellular spaces, respectively. Model input $u(t)$ is defined as:

$$u(t) = \begin{cases} D \cdot \delta(t) & \text{if } t = 0 \\ 0 & \text{otherwise} \end{cases}$$

where D denotes the amount of administered DOXO.

As it will be shown in Section V, *Model I* is not able to describe DOXO PK in MM cells well. Hence, further model structures have been investigated.

Model II: This structure represents an extension of *Model I*, and takes possible mechanisms of cell drug resistance into account. In particular, the model assumes a time-varying efflux rate from intracellular to extracellular space, $k_{EF}(t)$, defined as a linear function depending on either X_F, X_B

or X_I (described in Fig. 3b,c and d, respectively), which effectively yields three submodels to identify. Model equations are presented in equations (4) and (5).

$$k_{EF}(t) = k_{EF}X_i(t), \quad X_i \in \{X_F, X_B, X_I\}. \tag{4}$$

$$\begin{cases} \dot{X}_E(t) = k_{EF}(t)\frac{V_I}{V_E}X_F(t) - k_{FE}X_E(t) + u(t), \\ \dot{X}_F(t) = k_{FE}\frac{V_E}{V_I}X_E(t) - k_{EF}(t)X_F(t) - k_{BF}X_F(t), \\ \dot{X}_B(t) = k_{BF}X_F(t). \end{cases} \tag{5}$$

Model III and IV: As a variation of *Model II*, *Model III* and *IV* still hypothesize drug resistance but described by a threshold and saturation mechanism. Specifically, these phenomena are modeled with a Hill equation to analyze the relationship between the drug concentration and its kinetics [24]. Hence, model equations are (5) and (6):

$$k_{EF}(t) = \frac{V_{max}X_i(t)^{q-1}}{k_{th}^q + X_i(t)^q}, \quad X_i \in \{X_F, X_B, X_I\}, \tag{6}$$

with k_{th} (nM) denoting the X_I concentration at which the flux exiting from the intracellular space ($F_{EF}(t) = k_{EF}(t)X_I(t)$) is equal to 50% of its maximum value V_{max} (nM/hr). Parameter q represents the Hill coefficient that determines the sharpness of the transition and the slope of the dose response curve. Here we assume q equal to 1 or ≥ 2, for *Model III* and *IV*, respectively. Note that for $q = 1$ the Hill function is equivalent to the Michaelis-Menten equation [25]. It is worth mentioning that the performance of *Models II-IV* depending on either X_F, X_B or X_I is further investigated in section V.

IV. Model Identification

A. A priori identifiability

A priori identifiability is an essential step in system identification and mathematical model development. Global identifiability investigates the possibility of estimating a unique set of model parameters based on observations. Lack of global identifiability might lead to local optima problem, failing in convergence to a unique set of estimated parameters and, consequently, to noninterpretability of the obtained numerical solutions.

In the present work, the a priori identifiability of model candidates described in the previous section is investigated by DAISY (Differential Algebra for Identifiability of Systems), a software tool developed to check global identifiability of biological and physiological systems [26]–[28].

For all the *Models I-IV*, we assume that i) $X_I = X_F + X_B$ is the model output ii) D is the system input known by protocol (i.e., 200 nM or 450 nM) and iii) V_E and V_I are fixed parameters, i.e., V_E is known by protocol and V_I is calculated by multiplying the number of cell seeded by a single cell volume. On the other hand, the vector θ of unknown parameters (to be identified) is defined as

$$\begin{cases} \theta_{I,II} &= [k_{FE}, k_{EF}, k_{BF}] \\ \theta_{III} &= [k_{FE}, k_{BF}, V_{max}, k_{th}] \\ \theta_{IV} &= [k_{FE}, k_{BF}, V_{max}, k_{th}, q] \end{cases} \tag{7}$$

for *Models I,II*, *Model III* and *Model IV*, respectively.

Under these assumptions, *Models I-III* are a priori identifiable. Differently, a priori local identifiability is obtained for *Model IV*. More precisely, numerical analysis by DAISY provides q distinct solutions, i.e., with k_{th} assuming only one positive, one negative and a number of imaginary solutions depending on q. Nevertheless, k_{th} represents a concentration value, which clearly cannot be neither negative nor imaginary. Under this constraint, only one k_{th} solution is acceptable, therefore also *Model IV* results a priori globally identifiable.

B. System identification

The intracellular DOXO concentration, averaged over replicates, was measured for $t = 0, ...8$ hrs, for each of the four experiments (two DOXO dosages $\times$ two cell lines). In order to generalize each model with respect to drug dosage, we considered the measurement vector $y(t)$ as the merged intracellular concentration data obtained following both 200 nM and 450 nM DOXO administration, for the same cell line:

$$y(t) = X_I(t) = \left[X_I^{200}(t), X_I^{450}(t)\right]$$

Then, the measurement model is defined as

$$\hat{y}(t) = \hat{X}_I(t; \theta_i), \quad \theta_i : \{\theta_I, \theta_{II}, \theta_{III}, \theta_{IV}\}$$

where $\hat{X}_I(t; \theta_i)$ is the *i-th* model prediction for the total (i.e., sum of free and bound) intracellular compartment and θ_i is the parameter vector associated to the *i-th* model, defined in (7). In other words, for each model, a unique vector of model parameters was considered for predicting multiple dose-related concentration data.

Models I was identified by defining $y(t) = X_I(t)$ and applying Nonlinear Least Squares (NLS) to estimate the parameter vector $\hat{\theta}_i$ as follows

$$\hat{\theta}_i = \text{argmin RSS}(\theta_i) = \text{argmin } ||X_I(t) - \hat{X}_I(t; \theta_i)||^2$$

where RSS is the residuals sum of squares, i.e., the sum of squares of residuals between intracellular DOXO data and model prediction ($res(t) = y(t) - \hat{y}(t)$). A Maximum a Posteriori (MAP) estimator was used to identify *Models II-IV*, especially for reliably estimating k_{EF}, V_{max} and k_{th}

$$\hat{\theta}_i = \text{argmin} \left[||y - \hat{X}_I(t; \theta_i)||^2 + (\theta - \mu_\theta)' \Sigma_\theta^{-1} (\theta - \mu_\theta)\right]$$

where the second term represents the distance of the estimated parameters from their joint distribution, i.e., the parameter average vector μ_θ and covariance matrix Σ_θ.

Both NLS and MAP estimators were implemented in MATLAB 2020b (Natick, MA) using the *lsqnonlin* function, and the *ode45* solver was used to integrate the model differential equations. The initial conditions for θ_i were set to the respective estimates obtained in the preliminary work done in [23], while parameter lower bounds were set to zero, in order to exclude unrealistic values and to guarantee global model identifiability. A priori knowledge for V_{max} and k_{th} (*Models III* and *IV*) was derived from [29]. The same statistical information was

exploited to determine, by error propagation, the prior of k_{EF} (*Model II*), specifically its variance was determined as

$$var(k_{EF}) = \left(\frac{\partial k_{EF}}{\partial V_{max}}\right)^2 var(V_{max}) + \left(\frac{\partial k_{EF}}{\partial k_{th}}\right)^2 var(k_{th}) + 2\frac{\partial k_{EF}}{\partial V_{max}}\frac{\partial k_{EF}}{\partial k_{th}} cov(V_{max}, k_{th})$$

V_E was set at 100 µL by protocol, as the volume of one µ-Slide VI $^{0.4}$ well employed in the *in vitro* experiments. V_I was equal to 0.0703 µL or 0.1176 µL for MM1R and MOLP-2 cells, respectively, calculated by multiplying the number of cell seeded (5×10^4) by a single cell volume (1.41×10^{-6}µL or 2.35×10^{-6} µL, for MM1R and MOLP-2, respectively). The single cell volumes were calculated assuming a sphere shape, and an average diameter of 13.9µm or 16.5µm, for MM1R or MOLP-2, respectively. These values were experimentally determined, by averaging the diameters empirically measured in $\sim$150 cells for each cell line. DOXO dose was defined as the model input. In addition, in order to mimic the *in vitro* experiments, DOXO removal and medium replacement at $t =$ 3 hrs was simulated by forcing the extracellular state to zero ($X_E(3) = 0$).

C. Model assessment and comparison

Model selection was performed by assessing the capability of each model to predict the data and the numerical (a posteriori) identifiability of model parameters [25]. Model ability to predict the data was assessed by RSS. To note, RSS was also used to determine the best comparmental dependency, among X_F, X_B, X_I, regarding the intracellular efflux rate $k_{EF}(t)$ defined in *Models II-IV*.

Furthermore, in addition to a posteriori identifiability, the precision of parameter estimates, was assessed by percent coefficient of variation (CV), calculated as the ratio between the standard deviation (SD) of parameter estimates and the estimated parameter values ($\hat{p}$)

$$\text{CV} = \frac{\text{SD}}{\hat{p}}$$

Poor precision of an estimated parameter is concluded when its CV is above 100%.

It is worth noting that SD of estimated model parameters as well as the confidence interval (CI) of model prediction are obtained by bootstrap method [30]. In particular, a first round of model identification was performed on concentration data, providing both parameter estimates, model prediction and residuals time course. Then, we generated 1000 synthetic data (i.e., sum of initial model prediction and a bootstrap with replacement of the residuals) on which the model was re-identified. As a result, we obtained a population of 1000 estimated parameter vectors and model predictions, from which it was possible to calculate parameter SD and prediction CI.

If the previous criteria was satisfied, the most parsimonious model, describing the experimental data with the minimum number of parameters, was selected according to the Akaike Information Criterion (AIC, [31]) defined as:

$$\text{AIC} = \log\left(\frac{\text{RSS}}{n}\right) + \frac{(P+1)\ 2}{n}$$

where P is the number of parameters and n is the number of available samples. The best model was then selected as the one which better describes the data with the minimum number of model parameters (lowest AIC) followed by good precision (lowest CV).

V. Results

A. Efflux rate intracellular dependency

As detailed in the previous sections III and IV, different intracellular dependencies have been considered to model the efflux rate in *Models II-IV*, i.e., the configurations illustrated in Fig. 3b, c and d. Model comparison, in terms of model fit on both MM1R and MOLP-2 data, is provided in Fig. 4 and Table I. In particular, for both *Models II* and *IV*, the lowest RSS is reached when $k_{EF}(t)$ depends on X_B, while the lowest RSS using *Model III* is obtained when $k_{EF}(t)$ depends on X_F. These results are consistent among cell lines. These functional dependencies have been considered for a proper model structure comparison presented hereafter.

B. Model comparison and selection

Fig. 5 shows the performance of the candidate *Models I-IV* to predict both MM1R and MOLP-2 cell data. Both *Models I* and *III* fail to fit MM data. Specifically, for both cell line experiments, *Models I* and *III* systematically underestimate DOXO 200 nM data and poorly predict the uptake phase ($t \leq 3$ hrs) following DOXO 450 nM administration. On the other hand, model fit obtained with *Model II* is improved, specifically, it can be observed that low DOXO dose data are well predicted in both MM1R and MOLP-2 cells, while model performance slightly worsens when predicting high dose concentrations in MOLP-2 cells. Finally, *Model IV* outperforms in predicting both MM1R and MOLP-2 cell data at both DOXO concentrations. Similarly, among the four model candidates, *Models II* and *IV* provide best performance in terms of RSS and AIC (Table II): when related to MM1R, RSS and AIC values are slightly higher and lower, respectively, for *Model II* vs. *Model IV*; while, when related to MOLP-2, both RSS and AIC favour *Model IV*. For all *Models I-IV*, the parameters were estimated with good precision in terms of CV.

Given the above considerations, *Model IV* is preferred to *Model II* as it provides the best fit on DOXO data for both cell lines, in a parsimonious way and with precise estimated parameters. In addition, by considering a saturation-threshold formulation more realistic than a simple (i.e., non-saturating)

Table I: Summary results of *Models II-IV* comparing different k_{EF} functional dependencies

Model	Cell line	RSS (10^3 nM^2) X_F	X_B	X_I
Model II	MM1R	11.30	3.60	6.30
	MOLP-2	5.20	2.45	2.70
Model III	MM1R	43.32	83.20	110.80
	MOLP-2	22.99	28.04	33.68
Model IV	MM1R	10.57	3.37	5.98
	MOLP-2	4.03	1.69	2.15

This article has been accepted for publication in IEEE Transactions on Biomedical Engineering. This is the author's version which has not been fully edited and content may change prior to final publication. Citation information: DOI 10.1109/TBME.2023.3324017

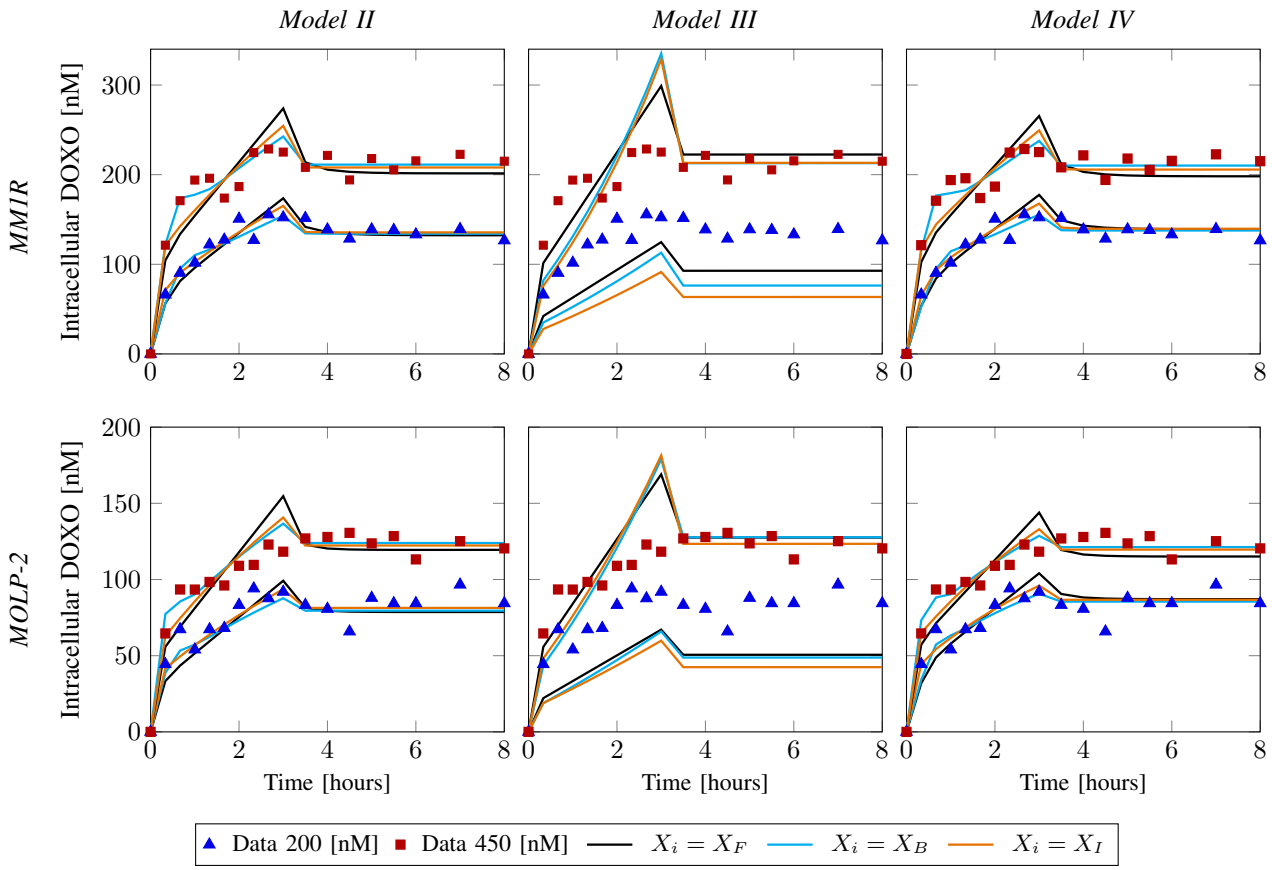

Figure 4: Intracellular DOXO concentration data measured following the treatment with DOXO 200 nM (*blue triangles*) or 450 nM (*red squares*) and model predictions obtained with *Model II* (*left*), *Model III* (*center*) and *Model IV* (*right*) with K_{EF} dependent on $X_i(t)$, where $X_i : \{X_F$ (*black*), X_B (*cyan*), X_I (*orange*)$\}$ in MM1R (*upper*) and MOLP-2 cell lines (*lower panels*).

linear relationship, *Model IV* also provides a biologically plausible description of $k_{EF}(t)$.

Parameter estimates obtained from *Model IV* identification on both MM1R and MOLP-2 cell data are reported in Table III (for sake of completeness, the complete results of estimated parameters for all model candidates are reported in the Appendix). Despite parameter estimates having comparable order of magnitude among cell lines, it is worth noting that DOXO PK in MOLP-2 is characterized by a faster (doubled) efflux rate V_{max} (which reaches the half saturation more promptly and at lower concentration k_{th}) and a faster entry into nucleus k_{BF}, resulting in a lower DOXO concentration compared to the PK profile observed in MM1R. A graphical comparison showing the different contribution of X_F, X_B, X_I in predicting MM1R and MOLP-2 data is reported in Fig. 6. Specifically, it can be observed how the intracellular DOXO concentration increases rapidly in the beginning of the uptake phase mainly due to X_F, which reaches its maximum value at $t = 0.68$ hrs or $t = 0.47$ hrs, in MM1R and MOLP-2 cells, respectively. Then, X_F gradually decreases until the end of the uptake phase ($t = 3$ hrs), after which it quickly decreases to zero. On the other hand, the bounded compartment X_B increases in the uptake phase following a slower dynamic, and then it stabilizes after DOXO removal.

Table II: Summary results of model comparison

Model	Cell line	$\overline{\text{CV}}$ [min, max] (%)	RSS (10^3 nM^2)	AIC
Model I	MM1R	21.13 [15.15, 24.14]	38.61	7.20
	MOLP-2	28.30 [19.64, 32.72]	17.58	6.41
Model II	MM1R	9.75 [7.77, 13.75]	3.60	4.83
	MOLP-2	23.96 [13.00, 37.59]	2.45	4.44
Model III	MM1R	12.41 [10.26, 14.93]	43.32	7.37
	MOLP-2	37.29 [16.53, 71.37]	22.99	6.74
Model IV	MM1R	17.51 [7.64, 34.69]	3.37	4.87
	MOLP-2	24.87 [11.68, 32.26]	1.69	4.18

Table III: Model IV parameters: mean values $\pm$ standard deviation and their precision (CV)

Cell line	k_{FE} (10^{-4} hr^{-1})	V_{max} (10^4 nM/hr)	k_{th} (nM)	q (dimensionless)	k_{BF} (hr^{-1})
MM1R	5.63 $\pm$ 0.43 (7.64%)	1.65 $\pm$ 0.57 (34.69%)	464 $\pm$ 108 (23.24%)	2.31 $\pm$ 0.29 (12.48%)	1.22 $\pm$ 0.12 (9.48%)
MOLP-2	6.15 $\pm$ 0.72 (11.68%)	2.39 $\pm$ 0.72 (30.16%)	231 $\pm$ 53 (23.05%)	2.82 $\pm$ 0.91 (32.26%)	2.18 $\pm$ 0.59 (27.20%)

This article has been accepted for publication in IEEE Transactions on Biomedical Engineering. This is the author's version which has not been fully edited and content may change prior to final publication. Citation information: DOI 10.1109/TBME.2023.3324017

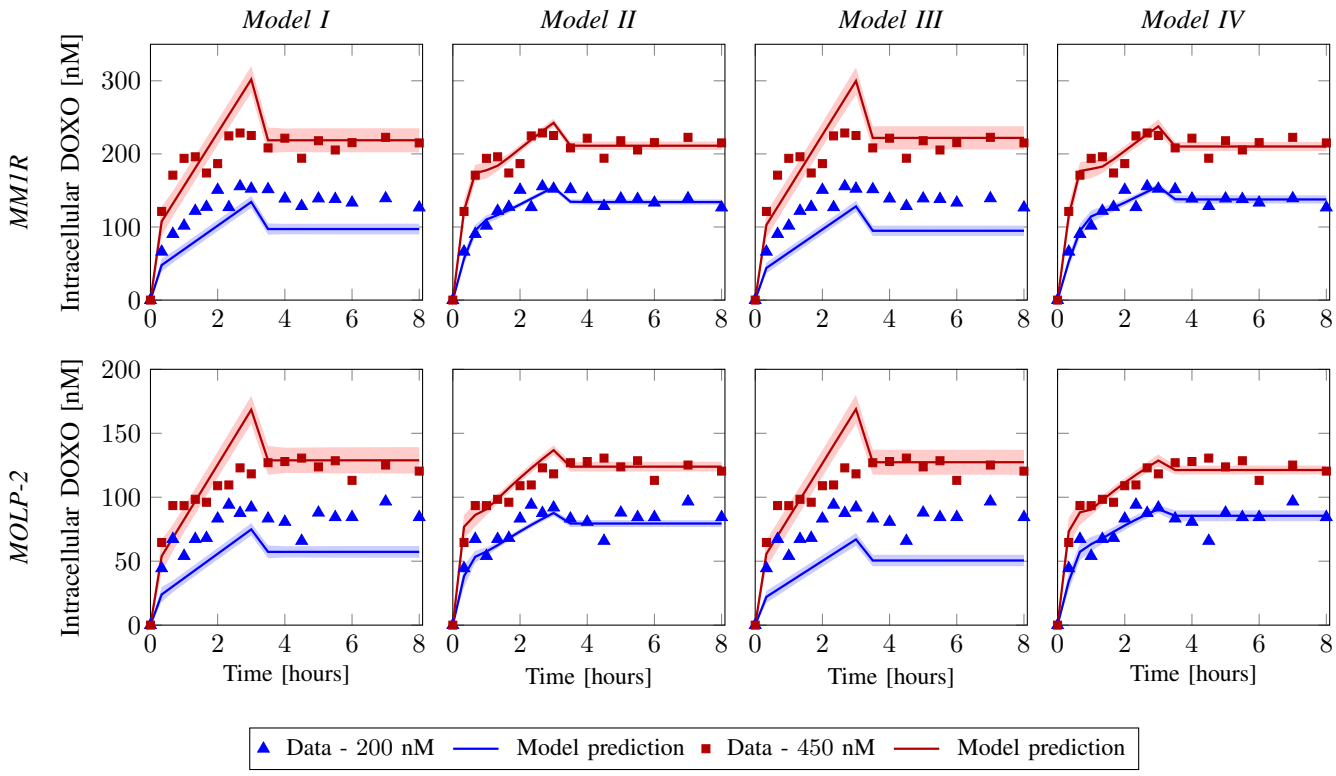

Figure 5: DOXO concentration measurements (*squares*) compared against predictions obtained with *Model I* (*left*), *Model II* (*middle left*), *Model III* (*middle right*) and *Model IV* (*right panels*) following the administration of DOXO 200 nM (*blue*) or 450 nM (*red*), in both MM1R (*upper*) and MOLP-2 cells (*lower panels*). Model predictions are reported as mean (*continuous lines*) and 95% confidence interval (*shaded area*).

VI. Discussion

A PK/PD simulation model of DOXO in MM cells would be highly desirable to support treatment optimization for an effective cancer therapy. Indeed, such a tool would allow exploring several treatment protocols that would be complex, time demanding and expensive to realize experimentally, and would provide a scalable approach for predicting MM response to DOXO PK *in vivo*. In this framework, it is clear that a reliable model, able to well describe DOXO PK in MM using precisely estimated model parameters, represents a key ingredient for providing a trustworthy drug exposure/response. The aim of the present work was to propose a model of DOXO PK in two MM cell lines (i.e., MM1R and MOLP-2) using intracellular DOXO concentration measures. This was achieved by developing and comparing different model structures. In particular, we started from the available *Model I*, previously developed from breast cancer data [12]. As shown in Fig. 4, this model was not suitable for predicting DOXO concentration in MM.

By looking at the data pattern, it can be noticed that the DOXO concentration seems to increase at different rates during the uptake phase, i.e., the increase is fast right after drug administration and slower after a certain delay. Based on this consideration, we speculated about possible drug resistance phenomena to be taken into account. In particular, it is well known that the DOXO effect is reduced in p-glycoprotein (p-gp)-expressing cells [29], [32], [33], so that

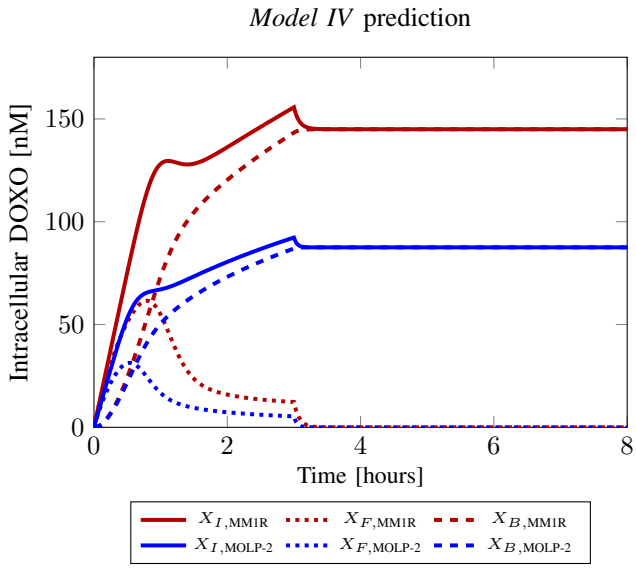

Figure 6: Predicted free (X_F, *dotted line*) DNA-bounded (X_B, *dashed line*) and total ($X_I = X_F + X_B$, *continuous line*) intracellular DOXO concentration following the administration of DOXO 200 nM in MM1R (*red*) and MOLP-2 (*blue*) cell lines.

DOXO may be actively effluxed from the cell, thus resulting in a drug-resistance mechanism. This process was implemented by modeling the cellular efflux rate (k_{EF}) with three different formulations: i) a linear dependency on DNA-bounded DOXO (*Model II*), ii) a saturation process, described by Michaelis-Menten equation, depending on free DOXO (*Model III*), and iii) a saturation-threshold mechanism, defined by Hill equation, depending on DNA-bounded DOXO (*Model IV*). The most suitable compartmental dependency was established for each of these models, by comparing, within the same formulation, the model predictions obtained by considering free, DNA-bounded, or total intracellular DOXO functional dependency.

Among the proposed models, only *Models II* and *IV* were able to satisfactorily fit the data. Actually, their prediction was very similar (especially when fitting DOXO data on MM1R cells) due to the fact that, given the estimated parameters (V_{max}, k_{th}, q), the linear $k_{EF}(t)$ approximates the Hill function well in the explored range of DOXO values. However, the saturation-threshold mechanism proper of *Model IV* appears more reasonable from a biological point of view. Thus, *Model IV* was selected as the one providing the best results in terms of both model prediction, parameter reliability and biological plausibility. In particular, it is worth mentioning how the selected model is able to capture the different PK profiles characterizing the two cell lines, as a result of a greater and more responsive drug resistance in MOLP-2 cells, in which the efflux rate saturates at a higher rate (V_{max} doubled in MOLP-2 vs. MM1R). To note, no DOXO PK characterizations has been previously done in MM, so that a direct parameter comparison is impossible. Nevertheless, the rate parameters for DOXO kinetics in breast cancer cells, as estimated with the similar model developed to describe DOXO PK in breast cancer [12], are lower than our estimates for MM, corresponding to the slower observed DOXO rise in breast cancer compared to MM. Thus, reliability and plausibility of our model are supported by precisely estimated parameters and, indirectly, by consistency with other studies.

Despite the satisfactory results, it is important to point out some considerations. First, given the experimental setup, it was not feasible to track cells over time. As such, all the modeling analysis relies on the assumption that DOXO distributes homogeneously among the cultured cells. Likely, this aspect would explain the observed DOXO variability within the same experiment. This aspect also suggested us not to consider the standard deviation of the data within the model identification process. Thus, all the data were equally weighted during the same model identification. This choice appears reasonable for the present analysis, in which only two DOXO dosages (with the same order of magnitude) have been evaluated. As stated in section II-B, the selected doses were such as to guarantee an appropriate reading of the DOXO signal without inducing early apoptosis. However, it is worth noting that the current data explored a limited range of DOXO concentrations, which affected the estimation of Hill parameters (especially k_{th}), i.e., the data range only covered the initial quasi-linear portion of the Hill function. Indeed, the contributions of linear vs. Hill k_{EF} (described by eq. 4 and 6, respectively) to the model fit were substantially identical, and the a posteriori covariance matrix revealed a high correlation between V_{max} and k_{th} (of 0.986 and 0.933, from identification on MM1R or MOLP-2 data, respectively). Nevertheless, the MAP estimation based on the previous study [29] allowed obtaining robust parameter estimates. Despite future experiments with higher DOXO doses that would allow further investigations of this limitation, it is reasonable to assume that a saturating efflux would be more realistic than a quadratic one, and, likely, more appropriate in possible *in vivo* settings, where higher DOXO amounts are likely to be used to compensate the drug metabolism. Moreover, the model does not assume any DOXO degradation, which was difficult to quantify due to the short experiment duration. Very preliminary results on DOXO pharmacodynamics [34] suggest a degradation time of $\sim$260 hrs, which supports the assumption of no degradation during the 8-hr experiments studied here.

In addition to the evaluation of further DOXO dosages, it would also be interesting to study DOXO PK under different treatment durations beyond the 3 hrs. Such analyses will allow evaluating potential model dependencies from treatment concentration and/or duration, thus possibly revealing model limitations, and consequently opening for model refinements. In addition, performing the same analysis on further cell lines, e.g. MM1s or KMS34 [21], would allow better assessment of the inter-cell line parameter variability. Finally, it is important to underline that this work describing DOXO PK from *in vitro* data represents a first step towards the development of a simulation model for preclinical testing of DOXO treatment. For this aim, the PK model will need to be integrated with a proper model of DOXO PD. Eventually, it may be part of a multiscale model incoorporating patient-specific data to simulate and optimize individualized treatment protocols and MM tumor response, similarly to what was proposed in [14].

VII. Conclusion

We developed a compartmental model able to describe DOXO PK in MM cells well. The model assumes that, after its administration to a cell culture, DOXO reversibly diffuses into cell cytoplasm and then it enters the nucleus, binding to the DNA and causing its damage. Differently from previous works done in breast cancer [12], the proposed model describes the DOXO efflux rate by a Hill function depending on DNA-bound DOXO, plausibly reflecting a p-gp mediated drug resistance mechanism [29].

The model has been identified on DOXO concentration data measured in both MM1R and MOLP-2 cell lines, following the administration of two distinct drug dosages. Model performance was satisfactory, showing its ability to predict DOXO data well, and resulting in the most parsimonious, yet biologically realistic, structure in terms of $\overline{\text{CV}}$, RSS and AIC. To the best of our knowledge, this work represents the first attempt to model DOXO PK in MM. Once coupled with an appropriate PD description of drug effects in MM cells, it will allow simulating the tumor response to different dosing protocols to inform and optimize preclinical testing of different drug regimens.

REFERENCES

[1] N. W. C. J. van de Donk, C. Pawlyn, and K. L. Yong, "Multiple myeloma," *The Lancet*, vol. 397, no. 10272, pp. 410–427, 2021. [Online]. Available: https://www.sciencedirect.com/science/article/pii/S0140673621001355

[2] A. J. Cowan *et al.*, "Global burden of multiple myeloma: a systematic analysis for the global burden of disease study 2016," *JAMA oncology*, vol. 4, no. 9, pp. 1221–1227, 2018.

[3] S. V. Rajkumar and S. Kumar, "Multiple myeloma: diagnosis and treatment," in *Mayo Clinic Proceedings*, vol. 91, no. 1. Elsevier, 2016, pp. 101–119.

[4] R. Eslick and D. Talaulikar, "Multiple myeloma: from diagnosis to treatment," *Australian family physician*, vol. 42, no. 10, pp. 684–688, 2013.

[5] R. Guilal *et al.*, "Clinical and paraclinical factors selection for multiple myeloma diagnosis," in *2019 International Conference on Advanced Electrical Engineering (ICAEE)*, 2019, pp. 1–6.

[6] A. Shafei *et al.*, "A review on the efficacy and toxicity of different doxorubicin nanoparticles for targeted therapy in metastatic breast cancer," *Biomed Pharmacother*, vol. 95, pp. 1209–1218, Nov 2017.

[7] N. Chowdhury *et al.*, "Targeted Delivery of Doxorubicin Liposomes for Her-2+ Breast Cancer Treatment," *AAPS PharmSciTech*, vol. 21, no. 6, p. 202, Jul 2020.

[8] T. A. Lawrie *et al.*, "Pegylated liposomal doxorubicin for relapsed epithelial ovarian cancer," *Cochrane Database Syst Rev*, no. 7, p. CD006910, Jul 2013.

[9] A. Palumbo *et al.*, "Bortezomib, doxorubicin and dexamethasone in advanced multiple myeloma," *Annals of Oncology*, vol. 19, no. 6, pp. 1160–1165, 2008.

[10] S. T. Duggan and G. M. Keating, "Pegylated liposomal doxorubicin," *Drugs*, vol. 71, no. 18, pp. 2531–2558, 2011.

[11] D. R. Barpe, D. D. Rosa, and P. E. Froehlich, "Pharmacokinetic evaluation of doxorubicin plasma levels in normal and overweight patients with breast cancer and simulation of dose adjustment by different indexes of body mass," *European Journal of Pharmaceutical Sciences*, vol. 41, no. 3-4, pp. 458–463, 2010.

[12] M. T. McKenna *et al.*, "A predictive mathematical modeling approach for the study of doxorubicin treatment in triple negative breast cancer," *Scientific reports*, vol. 7, no. 1, pp. 1–14, 2017.

[13] D. A. Drexler *et al.*, "Modeling of tumor growth incorporating the effect of pegylated liposomal doxorubicin," in *2019 IEEE 23rd International Conference on Intelligent Engineering Systems (INES)*. IEEE, 2019, pp. 000 369–000 374.

[14] X. Lai *et al.*, "Toward personalized computer simulation of breast cancer treatment: A multiscale pharmacokinetic and pharmacodynamic model informed by multitype patient data," *Cancer research*, vol. 79, no. 16, pp. 4293–4304, 2019.

[15] C. Ionescu, D. Copot, and R. De Keyser, "Modelling doxorubicin effect in various cancer therapies by means of fractional calculus," in *2016 American Control Conference (ACC)*, 2016, pp. 1283–1288.

[16] C. M. Ionescu *et al.*, "A minimal pkpd interaction model for evaluating synergy effects of combined nsclc therapies," *Journal of Clinical Medicine*, vol. 9, no. 6, p. 1832, 2020.

[17] M. Ghita *et al.*, "Model calibration of pharmacokinetic-pharmacodynamic lung tumour dynamics for anticancer therapies," *Journal of Clinical Medicine*, vol. 11, no. 4, p. 1006, 2022.

[18] K. K. Karukstis *et al.*, "Deciphering the fluorescence signature of daunomycin and doxorubicin," *Biophysical chemistry*, vol. 73, no. 3, pp. 249–263, 1998.

[19] R. E. Goldman-Leikin *et al.*, "Characterization of a novel myeloma cell line, mm. 1," *The Journal of laboratory and clinical medicine*, vol. 113, no. 3, pp. 335–345, 1989.

[20] Y. Matsuo *et al.*, "Establishment and characterization of new igd lambda type myeloma cell lines, molp-2 and molp-3, expressing cd28, cd33 antigens and the il-6 receptor." *Human Cell*, vol. 6, no. 4, pp. 310–313, 1993.

[21] V. Sarin *et al.*, "Evaluating the efficacy of multiple myeloma cell lines as models for patient tumors via transcriptomic correlation analysis," *Leukemia*, vol. 34, no. 10, pp. 2754–2765, 2020.

[22] C. A. Schneider, W. S. Rasband, and K. W. Eliceiri, "NIH Image to ImageJ: 25 years of image analysis," *Nat Methods*, vol. 9, no. 7, pp. 671–675, Jul 2012.

[23] A. Giaretta *et al.*, "Modeling pharmacokinetics of doxorubicin in multiple myeloma cells," in *2021 43rd Annual International Conference of the IEEE Engineering in Medicine & Biology Society (EMBC)*. IEEE, 2021, pp. 4374–4378.

[24] S. Goutelle *et al.*, "The hill equation: a review of its capabilities in pharmacological modelling," *Fundamental & clinical pharmacology*, vol. 22, no. 6, pp. 633–648, 2008.

[25] C. Cobelli and E. Carson, *Introduction to modeling in physiology and medicine*. Academic Press, 2019.

[26] G. Bellu *et al.*, "Daisy: A new software tool to test global identifiability of biological and physiological systems," *Computer methods and programs in biomedicine*, vol. 88, no. 1, pp. 52–61, 2007.

[27] M. P. Saccomani and L. D'angiò, "Examples of testing global identifiability with the daisy software," *IFAC Proceedings Volumes*, vol. 42, no. 10, pp. 48–53, 2009.

[28] M. P. Saccomani *et al.*, "Examples of testing global identifiability of biological and biomedical models with the daisy software," *Computers in Biology and Medicine*, vol. 40, no. 4, pp. 402–407, 2010.

[29] J. Kopecka *et al.*, "Insights into P-Glycoprotein Inhibitors: New Inducers of Immunogenic Cell Death," *Cells*, vol. 9, no. 4, Apr 2020.

[30] B. Efron and R. J. Tibshirani, *An introduction to the bootstrap*. CRC press, 1994.

[31] X.-S. Yang, *Introduction to algorithms for data mining and machine learning*. Academic press, 2019.

[32] M. T. McKenna *et al.*, "Leveraging mathematical modeling to quantify pharmacokinetic and pharmacodynamic pathways: equivalent dose metric," *Frontiers in physiology*, vol. 10, p. 616, 2019.

[33] M. E. Tome *et al.*, "P-glycoprotein traffics from the nucleus to the plasma membrane in rat brain endothelium during inflammatory pain," *Journal of Cerebral Blood Flow & Metabolism*, vol. 36, no. 11, pp. 1913–1928, 2016.

[34] D. Andrean *et al.*, "A pk/pd simulation model for supporting doxorubicin therapy in multiple myeloma," in *2023 Annual Congress of the European Association for Cancer Research (EACR)*, 2023, p. 35.

APPENDIX

This section presents the complete identification results investigating model comparison. Table IV reports parameter estimates and their precision (CV) obtained by identifying *Models I-IV* in MM1R and MOLP-2 cell lines.

Table IV: Estimated model parameters: mean values ± standard deviation and their precision (CV)

Cell line	*Model*	k_{FE} (10^{-4} hr^{-1})	k_{EF} (hr^{-1})* (hr^{-1} per nM)**	V_{max} (10^4 nM/hr)	k_{th} (nM)	q (dimensionless)	k_{BF} (hr^{-1})
MM1R	*I*	44.88± 10.84 (24.14%)	32.73 ± 7.89 (24.09%)	- -	- -	- -	0.85 ± 0.13 (15.15%)
	II	6.20 ± 0.48 (7.77%)	0.05 ± 0.01 (13.75%)	- -	- -	- -	1.14 ± 0.09 (7.74%)
	III	555.60 ± 71.99 (12.96%)	- -	52.8 ± 6.10 (11.49%)	1086 ± 111 (10.26%)	1 (fixed)	0.94 ± 0.14 (14.93%)
	IV	5.63 ± 0.43 (7.64%)	- -	1.65 ± 0.57 (34.69%)	464 ± 108 (23.24%)	2.31 ± 0.29 (12.48%)	1.22 ± 0.12 (9.48%)
MOLP-2	*I*	32.54 ± 10.59 (32.54%)	29.30 ± 9.59 (32.72%)	- -	- -	- -	1.05 ± 0.21 (19.64%)
	II	7.45 ± 1.59 (21.28%)	0.15 ± 0.06 (37.59%)	- -	- -	- -	1.62 ± 0.21 (13.00%)
	III	1244.4 ± 205.71 (16.53%)	- -	26.7 ± 11.5 (42.93%)	192 ± 137 (71.37%)	1 (fixed)	1.02 ± 0.19 (18.33%)
	IV	6.15 ± 0.72 (11.68%)	- -	2.39 ± 0.72 (30.16%)	231 ± 53 (23.05%)	2.82 ± 0.91 (32.26%)	2.18 ± 0.59 (27.20%)

*: k_{EF} measurement unit for *Model I*. **: k_{EF} measurement unit for *Model II*.